AGU PUBLICATIONS

JGR

Journal of Geophysical Research: Space Physics

RESEARCH ARTICLE
10.1002/2014JA020602

Key Points:
- Show quantitative maps of ground geomagnetic perturbations due to substorms
- Three vector components mapped as function of time during onset and recovery
- Compare/contrast results for different tilt angle and sign of IMF Y-component

Supporting Information:
- Readme
- Animation S1
- Animation S2
- Animation S3
- Animation S4
- Animation S5
- Animation S6

Correspondence to:
N. M. Pothier,
pothiern@gmail.com

Citation:
Pothier, N. M., D. R. Weimer, and W. B. Moore (2015), Quantitative maps of geomagnetic perturbation vectors during substorm onset and recovery, *J. Geophys. Res. Space Physics*, *120*, 1197–1214, doi:10.1002/2014JA020602.

Received 8 SEP 2014
Accepted 22 JAN 2015
Accepted article online 23 JAN 2015
Published online 20 FEB 2015

Quantitative maps of geomagnetic perturbation vectors during substorm onset and recovery

N. M. Pothier[1,2,3,4], D. R. Weimer[2,3], and W. B. Moore[1,2]

[1]Department of Atmospheric and Planetary Sciences, Hampton University, Hampton, Virginia, USA, [2]National Institute of Aerospace, Hampton, Virginia, USA, [3]Bradley Department of Electrical and Computer Engineering, Center for Space Science and Engineering Research, Virginia Tech, Blacksburg, Virginia, USA, [4]Department of Atmospheric, Oceanic, and Space Science, University of Michigan, Ann Arbor, Michigan, USA

Abstract We have produced the first series of spherical harmonic, numerical maps of the time-dependent surface perturbations in the Earth's magnetic field following the onset of substorms. Data from 124 ground magnetometer stations in the Northern Hemisphere at geomagnetic latitudes above 33° were used. Ground station data averaged over 5 min intervals covering 8 years (1998–2005) were used to construct pseudo auroral upper, auroral lower, and auroral electrojet (*AU**, *AL**, and *AE**) indices. These indices were used to generate a list of substorms that extended from 1998 to 2005, through a combination of automated processing and visual checks. Events were sorted by interplanetary magnetic field (IMF) orientation (at the Advanced Composition Explorer (ACE) satellite), dipole tilt angle, and substorm magnitude. Within each category, the events were aligned on substorm onset. A spherical cap harmonic analysis was used to obtain a least error fit of the substorm disturbance patterns at 5 min intervals up to 90 min after onset. The fits obtained at onset time were subtracted from all subsequent fits, for each group of substorm events. Maps of the three vector components of the averaged magnetic perturbations were constructed to show the effects of substorm currents. These maps are produced for several specific ranges of values for the peak $|AL^*|$ index, IMF orientation, and dipole tilt angle. We demonstrate an influence of the dipole tilt angle on the response to substorms. Our results indicate that there are downward currents poleward and upward currents just equatorward of the peak in the substorms' westward electrojet.

1. Introduction

Magnetic perturbations associated with large-magnitude geomagnetic storm events can damage and disrupt the operation of pipelines, power transmission lines, and sensitive electronics, such as communication and navigation satellite systems [*Lanzerotti*, 1979; *Boteler et al.*, 1998; *Lam et al.*, 2002]. The most severe effects are attributed to geomagnetically induced currents (GIC), "driven by rapid variations of ionospheric currents" [*Pulkkinen et al.*, 2003]. Reliable prediction of the spatial and temporal pattern of geomagnetic perturbations during space weather events would provide utility and satellite operators with valuable time to mitigate some of the most damaging effects.

Auroral substorms originating in the Earth's magnetotail are a major cause of the most intense GIC events [*Pulkkinen et al.*, 2003; *Viljanen et al.*, 2006]. The general consensus of the space physics community is that substorms are generated by magnetic reconnection following the accumulation of magnetic flux on open field lines, although there is not a universal agreement. The specific location where the reconnection originates and many other aspects of the substorm phenomena are topics of a multidecadal debate.

The global patterns of ground-level magnetic disturbances are often characterized in terms of the ionospheric equivalent current system. The variations in polar regions have been classified by two patterns designated as DP 1 and *DP* 2 [*Obayashi*, 1967; *Nishida,* 1968a, 1968b]. The *DP* 2 equivalent current system consists of twin vortices at high latitudes, having one vortex on the morning side and another on the evening side [*Clauer and Kamide*, 1985]. The *DP* 2 currents flow in the sunward direction across the middle of the polar cap to middle latitudes, crossing the auroral zone and closing through zonal currents. A concentration of the return current may occur in the auroral zone. The DP 1 disturbance is associated with substorms and is characterized by an intense auroral electrojet that grows rapidly during the substorm expansion phase. This westward directed current is typically located in the midnight sector, with return currents that flow through both the polar cap and the subauroral ionosphere [*Clauer and Kamide*, 1985].

The *DP* 2 system is mainly driven by solar wind interaction with the magnetosphere, while DP 1 results from unloading of energy in the tail of the magnetosphere during substorms [*Clauer et al.*, 1981, 1983]. The *DP* 2 system is predictable from knowledge of the solar wind as described below. This twin vortex system can become larger in magnitude and spatial size during strong disturbances. The DP 1 system is less predictable. The dipole tilt angle also has an effect on the response of ionospheric current systems to disturbances. A strong relationship between dipole tilt angle and the location of auroral substorm onset was found by *Liou et al.* [2001] and *Wanliss* [2006]. *Nowada et al.* [2009] found that the dipole tilt angle has an influence on the magnitude of the *AL* index.

Much progress has been made in understanding the relationship between the solar wind, with its embedded interplanetary magnetic field (IMF), and the directly driven magnetosphere-ionosphere system in general. Earlier work provided a description of the effects of the IMF on the equivalent current systems, as deduced from ground magnetometers [e.g., *Jørgensen et al.,* 1972; *Friis-Christensen et al.,* 1972, 1985; *Berthelier et al.,* 1974; *Friis-Christensen and Wilhjelm,* 1975; *Vennerstrøm and Friis-Christensen,* 1987]. Later measurement of electric fields using satellites or radar resulted in more progress, as exemplified by *Heppner and Maynard* [1987], *Rich and Hairston* [1994], *Ruohoniemi and Greenwald* [1996], and *Haaland et al.* [2007]. More recently, mappings of the field-aligned currents (FAC) as a function of the IMF have been derived from satellite magnetometer measurements [*Weimer*, 2001; *Christiansen et al.*, 2002; *Papitashvili et al.*, 2002; *Anderson et al.,* 2008, 2014]. The most recent work describes the global effects of auroral substorms on the equivalent current systems, also derived from ground magnetometers [*Gjerloev and Hoffman*, 2014]. However, to date, no comprehensive synthesis of the full spatiotemporal variation of ground perturbations due to substorms has been produced.

Other research has focused on the use of "first-principle" MHD computer simulations of the coupled solar wind-magnetosphere-ionosphere system. The publications on this topic are too numerous to list and beyond the focus of this paper; just a few examples are by *Raeder et al.* [2001], *De Zeeuw et al.* [2004], and *Wiltberger et al.* [2005]. While many regard physical simulations as the best way to model the geospace environment, and there have been promising results in GIC prediction, others question if it is possible to use MHD simulations to model the complexities of these geomagnetic perturbations on the ground due to substorms [*Pulkkinen et al.*, 2007]. Empirical models are necessary for verification and validation of numerical models.

Other predictive techniques use nonlinear filters to forecast geomagnetic perturbations as a function of IMF/solar wind drivers. A couple of examples are by *Gleisner and Lundstedt* [2001] and *Weigel et al.* [2002]. These are classified as empirical models, which do not require the large computing resources that the first-principle, numerical models require, and therefore, their solutions are obtained faster. Another type of empirical model uses spherical harmonics to represent the magnetic perturbations, as described in *Weimer* [2013].

Although magnetospheric substorms have a significant impact on sensitive technologies, they are poorly represented in current space weather models. A few studies have examined the relationship between the onset of magnetospheric substorms and their influence on ionospheric electric potentials and currents [e.g., *Weimer*, 1999, 2001]. The substorm current wedge model [*McPherron et al.*, 1973] that describes currents flowing in the magnetosphere and ionosphere, which produce the magnetic field perturbations during substorms, was developed using magnetic field data. *Kamide and Kokubun* [1996] also investigated mapping of the ionospheric current and electric field system using an inversion of ground magnetometer data. One result of their study was that at the peak of the electrojet current in the expansion phase, the electric potential pattern develops a high potential vortex near midnight, above 70° latitude.

Opgenoorth et al. [1983] had used measurements from a combination of radars, all-sky cameras, riometers, and an array of magnetometers, as well as a sounding rocket, to investigate the characteristics of a westward traveling auroral surge. They derived a localized map of electric and magnetic fields and currents over northern Scandinavia during the beginning of substorm expansion. Localized maps of the fields and currents have been derived by the "method of characteristics" [*Amm,* 1995, 2002] and the "elementary current method" [*Amm*, 2001]. A summary of these and other techniques is provided by *Amm et al.* [2008].

On a more global scale, *Fujii et al.* [1994] used measurements of electric and magnetic fields on the Dynamics Explorer 2 satellite, along with auroral images taken at a higher altitude on the Dynamics Explorer 1 satellite during multiple substorms. They derived characteristic maps of the large-scale field-aligned currents, electric fields, and electron precipitation in the nighttime sector.

Several other studies used similar techniques for mapping substorm electrodynamics, such as by *Gjerloev and Hoffman* [2002] and *Gjerloev et al.* [2007]. The most recent work by *Gjerloev and Hoffman* [2014] uses measurements from approximately 110 ground magnetometers during 116 substorms to create a statistical model of the magnetic perturbation on the nightside, at "the peak of a bulge-type substorm." Their results are presented in the form of an equivalent current system, through a 90° rotation of the magnetic field vectors. Most notably, they find that the westward electrojet shifts poleward as it passes through midnight and that there is a circular rotation in the current poleward of the electrojet. They propose a two-wedge current system linking the ionosphere to the magnetosphere to explain this phenomenon.

There have not been publications to date that show the full spatial and temporal variation of the substorm geomagnetic field perturbations on a global scale and for the entire duration of substorm expansion and recovery. We have accumulated a large enough data set (1998–2005) to construct a measurement-based description of the time-varying geomagnetic field at the surface of the Earth during magnetospheric substorms. The results implicitly include the effects of substorms on ionospheric electric potentials and currents, as well as any conductivity variations. Our analysis provides more detailed and quantitative maps, as a function of time, of both the distribution and magnitude of all three components of the magnetic perturbations. These maps show the effects of dipole tilt angle on substorm geomagnetic perturbations, complementing previous studies. Ultimately, the goal is to construct a descriptive model of geomagnetic perturbations that accurately accounts for the particular influence of substorms or, in other words, to derive a more quantitative portrayal of how the magnetic effects of the substorm current system vary in time and location.

In what follows, we detail the data sources and processing, event identification, event selection, spatial pattern fitting, and map generation. Section 2 describes our data and event management. Section 3 outlines our techniques for fitting and mapping the data. We describe our results in section 4 and discuss their implications in section 5.

2. Measurements

2.1. Data Sources

Measurements of the interplanetary magnetic field (IMF) are taken from the Magnetic Field Instrument and the Solar Wind Electron, Proton, and Alpha Monitor on the ACE satellite located at L1. Data obtained from these instruments were level 2 data in Geocentric Solar Ecliptic coordinates. The IMF measurements that were obtained in the upstream solar wind at approximately 240 R_E ahead of the Earth were rotated into Geocentric Solar Magnetospheric (GSM) coordinates and then averaged over 5 min intervals.

A solar wind velocity-dependent delay accounting for the propagation from ACE to the nose of the bow shock was added to the timing of the IMF data. An additional delay accounting for the propagation from the bow shock through the ionosphere was also added [*Weimer et al.*, 2010].

Ground magnetometer data were obtained from eight different data sources across the Northern Hemisphere: the International Real-time Magnetic observatory Network (INTERMAGNET), the Canadian Array for Real-time Investigations of Magnetic Activity (CARISMA), Japan's "210 MM Magnetometer Network" (GM210), the European International Monitor for Auroral Geomagnetic Effects (IMAGE), the Magnetometer Array for Cusp and Cleft Studies (MACCS), the Greenland magnetometer array, the WDC_UK (World Data Center, United Kingdom), and the Alaska Geophysical Institute Magnetometer Array (GIMA). Each data source contributed data from several ground magnetometer locations, hereafter referred to as stations. INTERMAGNET provided the majority of the data, as some of the other data sources are also part of the observatory network.

Data were obtained from a total of 149 stations. Due to larger gaps in the locations at lower latitudes, only data from stations with latitudes 33.4° and above were used, for a total of 124 stations. A list of stations with their corresponding corrected geomagnetic (CGM) apex latitudes and longitudes can be seen in Table 1. This list contains only the stations that were not included in the original list published by *Weimer et al.* [2010]. A map of the stations is shown in Figure 1, where the station locations are converted from geographic coordinates to geomagnetic apex coordinates [*Emmert et al.,* 2010]. In Figure 1, the magnetic apex latitude and longitude are used to plot positions on a polar graph. In later graphs, Figures 4–10, the positions are converted to a magnetic local time (MLT) hour angle for plotting and the data analysis. This MLT depends on the location of the Sun, so that the apex longitude of the subsolar point is at the top, where the MLT is 12. All

Table 1. Additional List of Station Codes, Locations, Latitudes (Corrected Geomagnetic), and Longitudes (Corrected Geomagnetic) for the Stations Used in the Analysis[a]

Code Location/Source	CGM Latitude (deg)	CGM Longitude (deg)
PGG Pangnirtung, MACCs	74.48	20.16
AVI Arctic Village, GIMA	68.58	263.28
FCH Fort Chipewyan	66.38	306.98
BET Bettles, GIMA	66.25	259.46
IVA Ivalo	64.89	108.53
KAR Karmoy, IMAGE	56.25	85.71
TAR Tartu, IMAGE	54.30	102.93
BOX Borok	53.84	113.88
NVS Novosibirsk	50.48	155.52
LVV Lvov	45.26	98.42
TUC Tucson	39.70	314.47
SUA Surlari	39.50	99.85
DLR Del Rio	38.70	326.27
MSR Mosiri	37.41	213.81
MMB Memambetsu	36.83	215.49
AQU L'Aquila	36.60	87.89
PPI Popov Island	36.43	204.11
EBR Ebro	34.79	76.55
BMT Beijing Ming Tombs	34.40	188.80
SPT San Pablo De Los Mon	33.41	72.17

[a]Original list is described by *Weimer et al.* [2010].

stations rotate around the magnetic apex pole as the universal time changes, while the electrodynamic patterns in the ionosphere are more stationary in the geomagnetic apex coordinates.

The original data had 60 s resolution but have been reduced to 5 min averages for the purpose of this study. Baseline, quiet levels were subtracted from each component for every station, as described by *Weimer et al.* [2010]. For this study, data from an additional 4 years have been processed in the same manner and appended to the *Weimer et al.* [2010] database, resulting in 8 years of processed data.

2.2. Data Processing

All data obtained from ground magnetometer stations were initially converted into a common flat-file format before further processing. Magnetometer data were obtained in two major sets: one for the years 1998–2001 (used by *Weimer et al.* [2010]) and one set that was processed later, for the years 2002–2005. The majority of stations had data in both time periods, but a small number had ceased operation, while a few stations at other locations had commenced measurements.

All magnetometer data were automatically checked for values that were not within a reasonable range, due to the various instrumental, transmission, and processing errors that result in "spikes" or otherwise unusable values. Then every month of data from each station for 1998–2005 was visually checked for other obvious indications of faulty values, which were removed. After the subtraction of background levels and a translation of the three vector components into local corrected geomagnetic coordinates, the data were reduced to 5 min averages for the entire 8 year period. Time-delayed solar wind and IMF measurements from the ACE satellite were concatenated into 5 min time steps having matching time stamps for the entire 8 year period. Since validated level 2 measurements from ACE commenced on the 36th day of 1998, this is the time at which the data compilation begins.

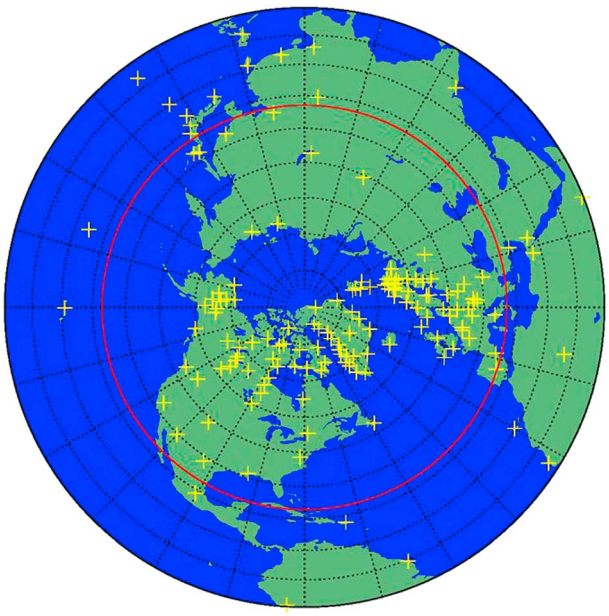

Figure 1. Map of station locations. Points poleward of the red line (at 33° latitude) were used in our analysis.

Dipole tilt angles and solar positions were calculated for all time steps in the 8 year period, applicable to all stations. Every station's corrected geomagnetic (CGM) apex latitude and longitudes were derived from their geographic coordinates and the

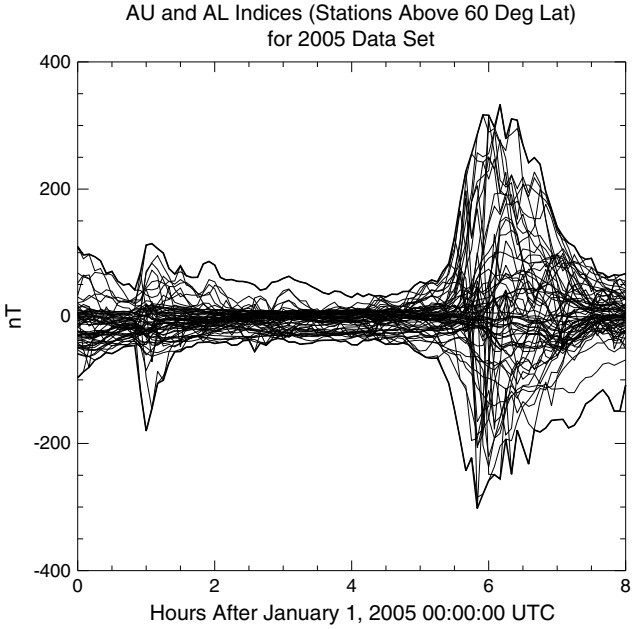

Figure 2. North–south component of all stations above 60° latitude, superposed, with upper and lower limits of the stations in bold. Plots only show the first 8.5 h of January as an example.

magnetic local time (MLT) of each station at every time step was derived from the longitudes of the station location and the subsolar point. The processing of the solar wind and IMF data, including time delays, and the ground magnetometer data are described in detail by *Weimer et al.* [2010].

2.3. Substorm Event Selection

For this project, we required a list of substorm onset times for the entire 8 year period. Ideally, auroral images from polar-orbiting satellites [*Gjerloev et al.*, 2004], combined with ground-level Pi2 pulsations [*Hsu and McPherron*, 2002], should be used to verify substorm occurrence. The latter requires 1 s resolution or better magnetometer measurements taken within auroral latitudes (approximately 50–70°) near midnight, and these data are not widely available. A list of substorm onsets obtained from *Frey et al.* [2004] was examined to see if it would be useful for this study; unfortunately, this list was found to have fewer cases than needed for our purpose. An independent substorm list published by *Newell and Gjerloev* [2011] was not yet available when the majority of the work that is reported here had already been completed. Out of necessity, the substorm list for this project was derived solely from the characteristics of auroral electrojet indices derived from our data.

Pseudo *AL*, *AU*, and *AE* indices were generated at the 5 min cadence for the entire 8 year period. For convenience, we refer to these as simply *AL**, *AU**, and *AE**, to indicate that they are not the official auroral electrojet indices from Kyoto. The *AL** and *AU** indices were derived from the lowermost (*AL**; usually negative) and uppermost (*AU**) range of magnetic field data from all stations in our data set with latitudes greater than or equal to 60°. The official indices are calculated with a fixed set of stations, fewer in number, within latitudes that are constricted to the auroral zone only (19–30° from the magnetic pole) [*Davis and Sugiura*, 1966; *Mayaud*, 1980]. Figure 2 is an example of the north–south component of all stations with latitudes greater than 60° for the time period from 0:00 to 8:00 UT on 1 January 2005, superposed. The upper limit of all stations was used to derive the *AU** index, and the lower limit of these stations was used to derive the *AL** index; these limits are shown as bold lines.

In order to generate the list of substorm events, we developed an automated selection algorithm to identify candidate substorm events as follows: At each 5 min time step, the program found the value of $|AL^*|$ at 25, 30, and 35 min forward in time. Exponential substorm curves, as described by *Weimer* [1994], that reach a peak at these time after onset were multiplied by a constant, so that their peaks matched the measured values of $|AL^*|$. These curves were compared to the measured $|AL^*|$ for 3 h intervals, computing the variance and standard deviation from their difference. If the lowest standard deviation of the three curves was less than 40% of that value, then the event was considered a candidate for consideration, provided that the peak in $|AL^*|$ was at least 100 nT. The 40% factor was determined by trial runs with small subset of data that included substorms that were first identified through an inspection of the magnetometer data. This scale factor obtained the best accuracy on detections without too many false positives. This process resulted in a candidate list that contained 4815 possible substorm onset times, or approximately 51 per month. These criteria are somewhat more selective than the automated search of *Newell and Gjerloev* [2011], which resulted in an average of ~150 substorms per month. Fifty-seven percent of the events in our substorm list are also in the Newell-Gjerloev list, some having exactly the same onset times, others differing by several minutes.

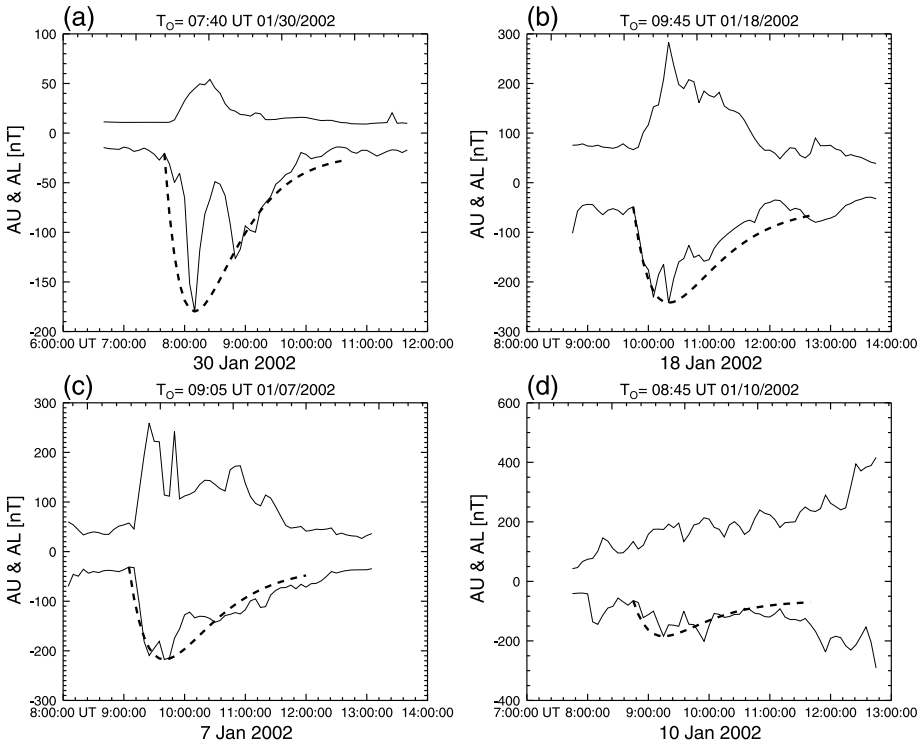

Figure 3. (a–c) Examples of cases where a substorm was identified. The dotted lines show the outline of the curve that the automated program used to calculate a match with the "canonical substorm time series [*Weimer*, 1994]." Example of a case where the onset time required a manual adjustment by a few minutes. (d) Example of a case where the automated program had marked a time as having a substorm onset, but it was rejected in the visual check.

Tanskanen et al. [2011] had also used an automated method to identify substorms from ground-based magnetic field measurements. Over a 16 year period, 550 substorms were observed per year, on average. This number, about 46 substorms per month, is similar to our result.

The process was sufficiently flexible to allow for significant departure from the exponential curve, due to the rapid magnetic field variations that result from chaotic turbulence in the ionosphere and sharp conductivity variations [*Pulkkinen et al.*, 2006]. Example events are shown in Figures 3a–3c. The dotted lines show the outline of the curve that the automated program had used to calculate a match with the "canonical substorm time series [*Weimer*, 1994]." The solid lines show the actual *AU** and *AL** indices.

The final step in the generation of the new list of substorm onset times was a visual inspection of the *AL** and *AU** curves for all 4815 events, to confirm that each event showed strong evidence of substorm signatures. Key factors that were checked for included (1) a simultaneous increase in *AU** and decrease in *AL**, the signature of a growth phase prior to onset. The distance between the *AL** and *AU** curves is allowed to decrease slightly just before onset, as is commonly observed (refer to Figure 2). (2) A rapid decrease in the *AL** index, having a (negative) peak occurring about 25–40 min after onset, followed with a slower rise over the next hour, or longer. (3) The magnitude of the *AL** index is generally greater than the *AU** index, particularly for irregularly shaped spikes. The possibility that the *AL** and *AU** indices were roughly the same size for the rise and decay in both curves was allowed, as long as they had identifiable expansion and longer recovery periods.

The automated routine occasionally generated false positives, where the *AL** index would decrease suddenly and then fluctuate more or less around a negative value, having no clear recovery phase. It is assumed that this occurs when the solar wind's electric field suddenly increases and stays high, such as when the *Z* component of the IMF transits from positive to negative and/or the velocity increases. Such events were not included in the final substorm list. An example of a rejected event is shown in Figure 3d.

In some cases, the onset times that were determined by the automated preprocessing routine did not match the visual determination, in which case the onset times were manually adjusted, to an accuracy of ±5 min.

Substorm onsets in the original list that did not meet the criteria specified were removed from the list during the visual inspection. The revised list contained 3123 substorms over the 8 year period.

We note that these criteria are subject to individual interpretations and also note that there is not likely to be unanimous agreement on these criteria among the community of substorm researchers. We also note that our final list is not guaranteed to contain every substorm that occurred, but an effort was made to eliminate false positives.

3. Mapping Substorm Influence on Ground Geomagnetic Perturbations

From the magnetic field measurements for 1998–2005, we have produced contour maps of the mean geomagnetic perturbations produced by substorms. The data were first organized prior to analysis by sorting the events according to the peak magnitude of the $|AL^*|$ index, corresponding to the most negative value measured during the expansion phase. Events were divided into four categories according to the maximum value of $|AL^*|$; these bins covered the ranges of 100–300, 300–500, 500–700, and 700–1000 nT.

It has been well known for quite some time that the IMF affects the large-scale morphology of the electric fields and currents in the high-latitude ionosphere [*Jørgensen et al.,* 1972; *Friis-Christensen et al.,* 1972, 1985; *Berthelier et al.,* 1974; *Friis-Christensen and Wilhjelm*, 1975; *Vennerstrøm and Friis-Christensen*, 1987; *Heppner and Maynard*, 1987; *Rich and Hairston*, 1994; *Ruohoniemi and Greenwald*, 1996; *Weimer*, 2001; *Christiansen et al.*, 2002; *Papitashvili et al.*, 2002]. The IMF is dominated by a sector structure that controls the large-scale variations in the *Y* component in the dawn-dusk direction perpendicular to the Earth-Sun line. Changes in the orientation of the IMF between sectors of different polarity are known to be responsible for large geomagnetic effects in the polar cap [*Friis-Christensen et al.*, 1972]. *Østgaard et al.* [2004] had found that IMF clock angle affects auroral substorm features. It is expected that large-scale electrodynamic patterns under the control of the IMF influence the spatial distributions of the currents that grow and subside during substorms. Therefore, our data are further divided into bins according to the sign of the IMF *Y* component in order to investigate the corresponding magnetic response during substorms. The two bins are designated according to the IMF clock angle in the GSM *Y-Z* plane, one for negative *Y* (clock angle $>$ 180°) and one for positive *Y* (clock angle $<$ 180°). Although it is well known that the *Z* component largely influences the magnitude of the cross-polar cap potential, as well as the substorm growth phase, it is often in transition during substorms, and therefore, the *Z* component is not a good parameter for sorting. Due to the simultaneous partitioning by other parameters, there are only sufficient data for a further division of events into these two bins according to IMF orientation.

In addition to dividing the event list according to the substorm magnitude and IMF B_Y polarity, the dipole tilt angle effects are investigated as well. This dipole tilt is the angle between the GSM *Z* axis and the dipole axis and it is the rotation angle that translates from the GSM to solar magnetic coordinate systems [*Hapgood*, 1992]. It is the complement of the angle between the magnetic dipole axis and the Earth-Sun line. This angle varies yearly by ±22.44° and corresponds to the seasons that are experienced in each hemisphere. There is an additional daily variation of ±10.2° (2005 epoch) that is superimposed due to the movement of the magnetic pole around the rotational pole. Since the dipole tilt angle indicates how much of the geomagnetic polar cap is illuminated, it has a strong control over ionospheric electric potentials and field-aligned currents [*Heppner and Maynard*, 1987; *Rich and Hairston*, 1994; *Christiansen et al.*, 2002]. Additionally, *Wanliss* [2006] has shown that dipole tilt angle does influence substorm onset location. One reason may be that this angle between the dipole axis and the solar wind flow has a strong influence on the downstream configuration of the magnetosphere and magnetotail.

For this study, the bins that were used for the dipole tilt angle were −33° to −13°, −10° to +10°, and +13° to +33°. These bins correspond to data taken over a range of dates that are centered on the winter solstice, both equinoxes, and summer solstice in the Northern Hemisphere. Within the middle range of tilt angles, we make no distinction between spring and fall. As time progresses between these astronomical events, the number of daily observations that are contained within these bins gradually changes, decreasing in one while increasing in another. Elsewhere in this paper, these tilt angle bins may be more conveniently referred to by the corresponding labels "winter," "equinox," and "summer," where the association with the given tilt angle ranges is implicitly understood, even though the dates of the observations may lie outside the conventional definitions of those terms.

To summarize the data sorting, the events were divided into four bins according to peak |*AL**| magnitude, further divided into two according to the IMF polarity, and divided three more ways by dipole tilt angle. Following this division, the more rare events having |*AL**| magnitude over 700 nT were too few in number to produce useful results, resulting in the elimination of this category. For convenience, the first three magnitude ranges are referred to as small- (100–300 nT), medium- (300–500 nT), and large-sized (500–700 nT) substorms.

We use a spherical cap harmonic analysis (SCHA) [*Haines*, 1985] to parameterize the spatial dependence of the ground-level magnetic perturbations. Each of the three vector components of the perturbation, ΔB, is computed separately. Each component is represented with a SCHA series defined as

$$\Delta B_x(\Lambda,\varphi) = \sum_{k=0}^{16} \sum_{m=0}^{3<k} P^m_{n_k(m)}(\cos\Lambda)\left(g^m_k \cos m\varphi + h^m_k \sin m\varphi\right) \quad (1)$$

where Λ represents colatitude in geomagnetic apex coordinates, φ is the MLT angle, and $P_{nk}(m)$ is an associated Legendre function with integer order m and non-integer degree. This non-integer degree is a function of both an integer parameter k (acting as degree) and the order m and is designated as $n_k(m)$. This notation is the same as that used by *Haines* [1985]. The value of this degree is also controlled by the size that is chosen for the polar cap half-angle Θ_o, and additionally, odd pairings of k and m (the difference between k and m is odd) produce a zero value at the boundary, and even pairings of k and m have a zero derivative. We use an even k-m pairing to produce a more stable solution near the lower latitude boundary, where the density of stations is lower. The harmonic series coefficients in (1) are computed from measurements using a least squares error fit that follows the same methodology described by *Weimer et al.* [2010]. The maximum values of k and m used in the series expansion are the same as those used by *Weimer et al.* [2010] and were chosen to resolve the global-scale variations in the perturbations, while limiting the amount of noise due to statistical fluctuations and variable gaps in the latitudinal spacing between the ground stations. The same number of coefficients is used for all maps.

While *Weimer et al.* [2010] had shown fits for latitudes poleward of 60° in order to show more detail at high latitudes, the results shown here are extended down to 33.4° in order to include midlatitude (30–50°) variations in the substorm mappings. At lower latitudes, there are multiple gaps in station coverage, on the order of 3°, that significantly limit spatial resolution if a larger cap size is used.

As discussed in the introduction, the ground-level magnetic variations in polar regions are considered to have two primary components, one of which is controlled by the IMF and is somewhat predictable from solar wind upstream measurements [*Weimer*, 2013]. Since the goal is to more accurately quantify the more unpredictable magnetic perturbations during substorm unloading, we would like to remove the driven component from the measured values. To avoid introducing added complexity, we have removed the best fit magnetic field at all stations at substorm onset (time = 0), for each set of selected events. These fits of the patterns at the time of onset are subtracted from the fit results at subsequent time steps, within each set. The subtraction operation is performed on the spherical harmonic coefficients before the maps are generated. An example of this technique is shown in Figure 4, which shows maps of the northward component of the geomagnetic perturbations for $-B_Y$ IMF (clock angle = 270°) and dipole tilt angle of 0° (equinox). The measurements are from medium-sized substorms having their greatest |*AL**| index in the range of 300–500 nT. Figures 4a and 4b show the raw data points and fits of the substorm perturbations at 30 min after substorm onset (time = 30 min). Figures 4c and 4d similarly show the data and fits at the time of onset (time = 0 min). Figure 4e shows the fit at 30 min after substorm onset, with the baseline (time = 0 min) subtracted out.

The initial fit in each group corresponds to the mean geomagnetic disturbance pattern that was in place at the time of onset. The solar wind and IMF may be changing after the time of onset and could produce changes in the electric fields and currents that are not directly related to the substorm current system. Unless these changes are correlated to substorm onset, growth, and recovery, they should average out to be zero over many events. The procedure that is used here is an approximation, as it assumes that the effects of these post-onset changes in driving conditions do not significantly alter the maps that are obtained.

4. Results

Results from the least squares fits of the geomagnetic perturbations related to the substorm component following onset are shown in Figures 5–10. All figures have three plots containing the contour maps of the

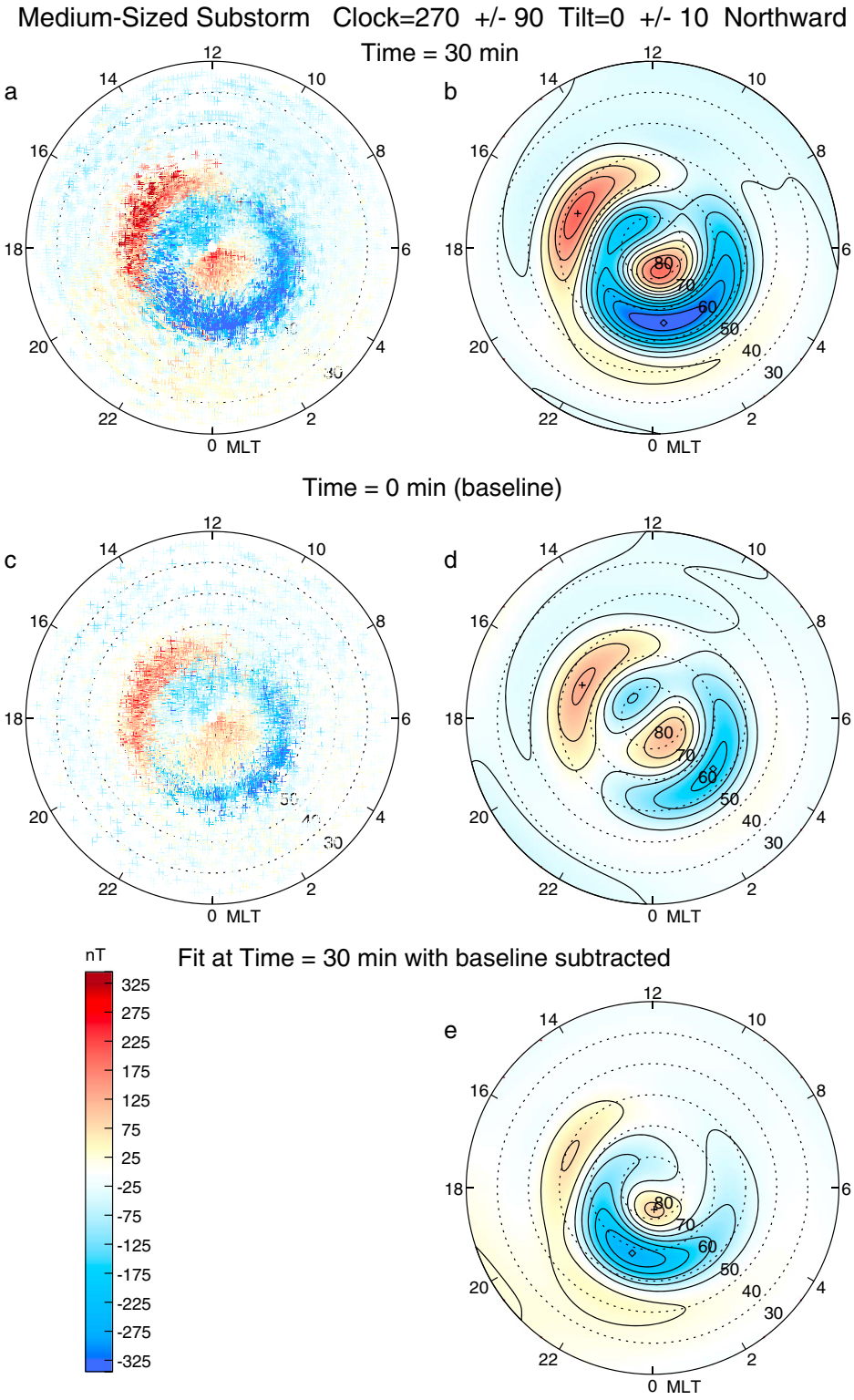

Figure 4. Maps of geomagnetic perturbations for a clock angle of 270° ($-B_Y$ IMF) dipole tilt angle of 0° (equinox) for the northward component. The measurements are from substorms having their greatest $|AL^*|$ index in the range of 300–500 nT. (a) The raw data points and (b) fits of the substorm perturbations at 30 min after substorm onset (time = 30 min). (c and d) Same as Figures 4a and 4b but for data at the time of onset (time = 0 min). (e) The fits at 30 min after substorm onset, with the baseline (time = 0 min) subtracted out.

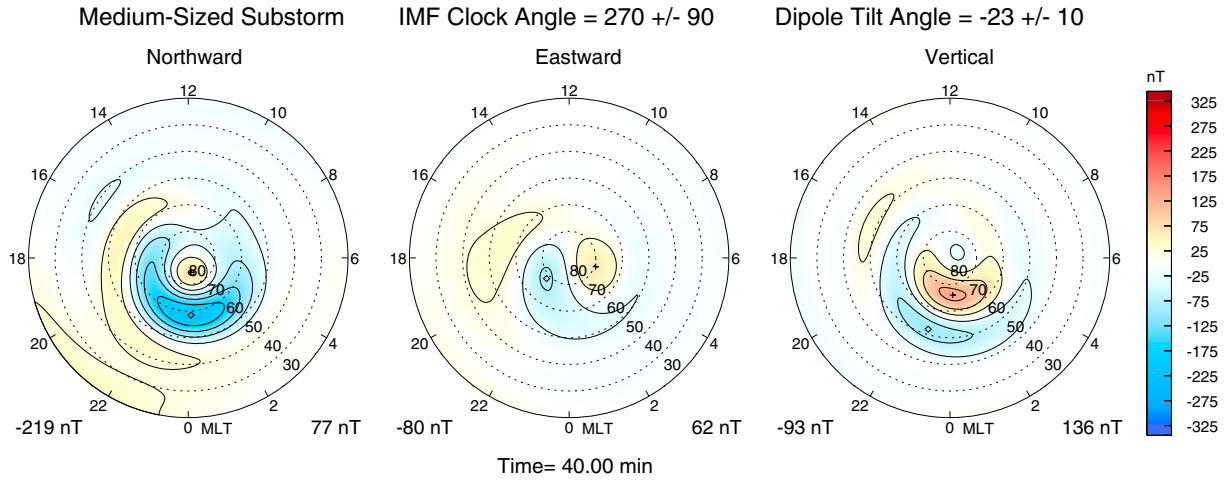

Figure 5. Maps of geomagnetic perturbations for a clock angle of 270° ($-B_Y$ IMF) and dipole tilt angle of 0° (equinox). The measurements are from substorms having their greatest $|AL^*|$ index in the range of 300–500 nT and taken at 40 min after onset of the expansion phase. Each of the three vector components is shown. These plots show the results of least error fits using spherical cap harmonics, with the baseline (time = 0 min) removed.

SCHA-derived values, where the fit at the time of onset has been subtracted from the fits at later times. From left to right, the plots show results for the northward, eastward, and vertical components, respectively. The numbers at the lower left-hand and right-hand sides of each plot indicate the minimum and maximum perturbations, respectively.

Our sorting of the data allows us to show the variations in the DP 1 system as a function of location for various dipole tilt angles and IMF clock angle ($-B_Y$ and $+B_Y$), as shown in Figures 5–10. As mentioned earlier, the graphs have been produced for substorms of different magnitude, at 5 min time steps from onset through recovery. To save space, we show only these plots for results obtained from substorms with an AL^* index in the range of −300 to −500 nT, as determined by the minimum value during each event. Since the timing of the peak of the expansion phase, as determined from the statistical fits, was found to vary slightly with tilt angle, ranging from 30 to 40 min, the maps at times 40 min after onset are shown for the sake of comparison. Animations showing the evolution of the field from onset through recovery for other magnitudes, dipole tilts, and IMF orientations are available in the supporting information.

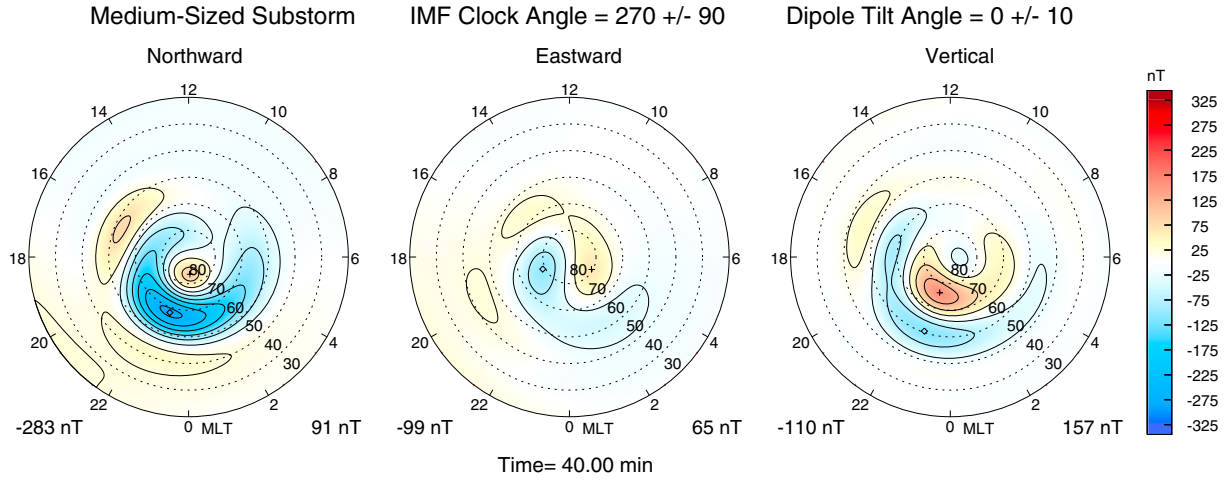

Figure 6. Maps of geomagnetic perturbations for a clock angle of 90° ($+B_Y$ IMF) and dipole tilt angle of 0° (equinox). The format of the figure and the other data selection conditions are the same as in Figure 5.

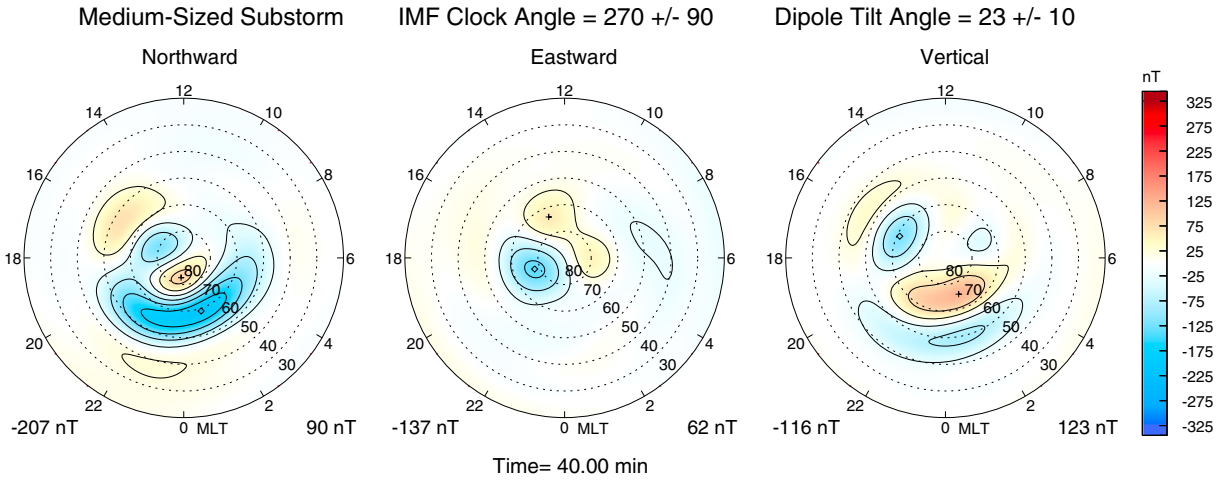

Figure 7. Maps of geomagnetic perturbations for a clock angle of 270° ($-B_Y$ IMF) and dipole tilt angle of −23° (winter). The format of the figure and the other data selection conditions are the same as in Figure 5.

4.1. Variations due to Season

When we examine the differences in the maps for the seasons (Figures 5, 7, and 9, and 6, 8, and 10), we notice that the most significant spatial changes among the seasons in both IMF $+B_Y$ and IMF $-B_Y$ are evident in the summer cases, for the eastward and vertical components. The locations of the dominant features of all three components in the winter and equinox cases tend to be roughly the same, although some variation in magnitude exists. In the summer case, however, we see features that are slightly less distinct and shifted than when compared to the other two cases, particularly for the vertical component. A shift toward postmidnight is particularly evident for the vertical component in Figure 9, for the $-B_Y$ IMF case. Additionally, in going from positive to negative tilt angles, there is a slight shift to higher latitude, on the order of 1–2°.

Intuitively, it would be expected that the magnetic perturbations should be stronger when the tilt angle is positive (near summer), since the additional solar illumination causes the ionospheric conductivity to be higher. But this is not always the case, as we find that perturbations are often stronger near equinox. The perturbations may be even stronger with negative tilt angles, as shown in Figure 8 for IMF $+B_Y$ (clock angle at 90°), contrary to expectations. It appears that enhancements to the conductivity within the nightside auroral oval, due to particle precipitation, tend to be the greatest when the tilt angle is negative and the conductivity within the polar cap is lower.

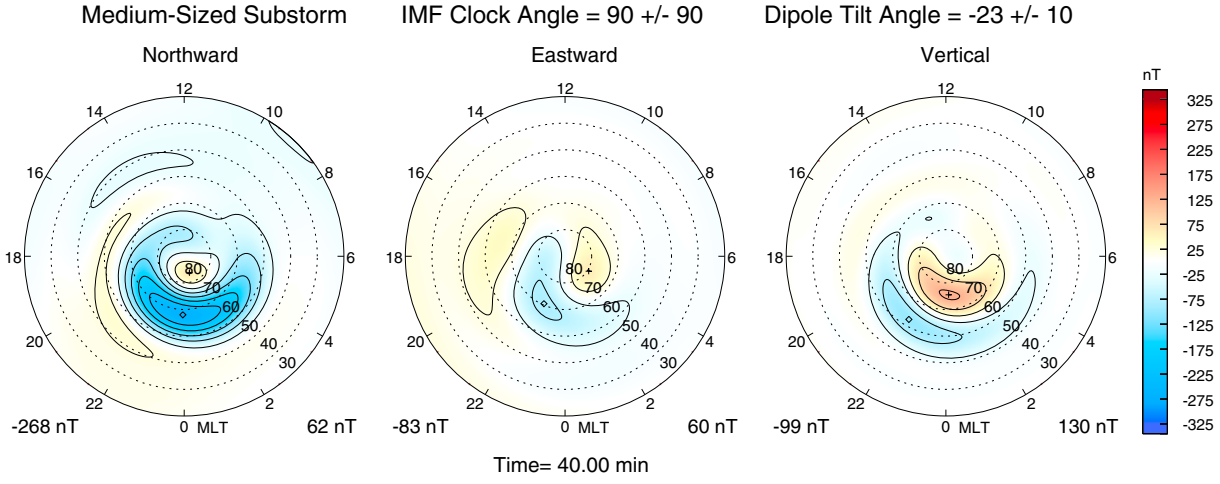

Figure 8. Maps of geomagnetic perturbations for a clock angle of 90° ($+B_Y$ IMF) and dipole tilt angle of −23° (winter). The format of the figure and the other data selection conditions are the same as in Figure 5.

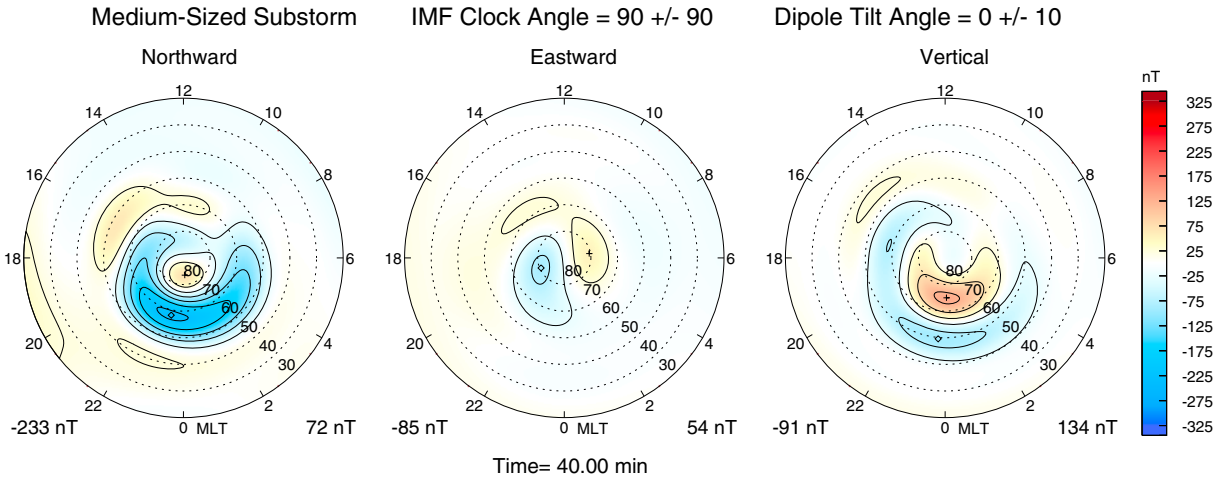

Figure 9. Maps of geomagnetic perturbations for a clock angle of 270° ($-B_Y$ IMF) and dipole tilt angle of 23° (summer). The format of the figure and the other data selection conditions are the same as in Figure 5.

4.2. Variations Controlled by IMF B_Y

If we compare the variations due to IMF B_Y (Figures 5–10), we see that the dominant features are generally very similar in location for all three components. The strength of these features varies a little between $+B_Y$ and $-B_Y$; the dominant features are stronger in the $-B_Y$ case for both the equinoxes and summer (Figures 5, 6, 9, and 10, respectively), for all three components. This suggests that the orientation of the IMF does not matter very much when it comes to the location of the greatest perturbations; however, it does have some effect on the magnitude of the greatest perturbations.

4.3. Substorm Time Evolution

Several animations describing the evolution of substorms as a function of time are presented in the supporting information, in addition to the variations due to season and IMF orientation comparisons discussed above. Time evolutions are presented in order to show a comparison between IMF $-B_Y$ and IMF $+B_Y$, summer, equinox, and winter. Also included are animations for three different groups of substorm magnitude, as determined by the most negative value of the *AL** index that was detected in each substorm. Each animation shows the 90 min lifecycle of a substorm, including the expansion phase and recovery phase. In each animation, the best fit maps of the magnetic field at the time of onset were subtracted from

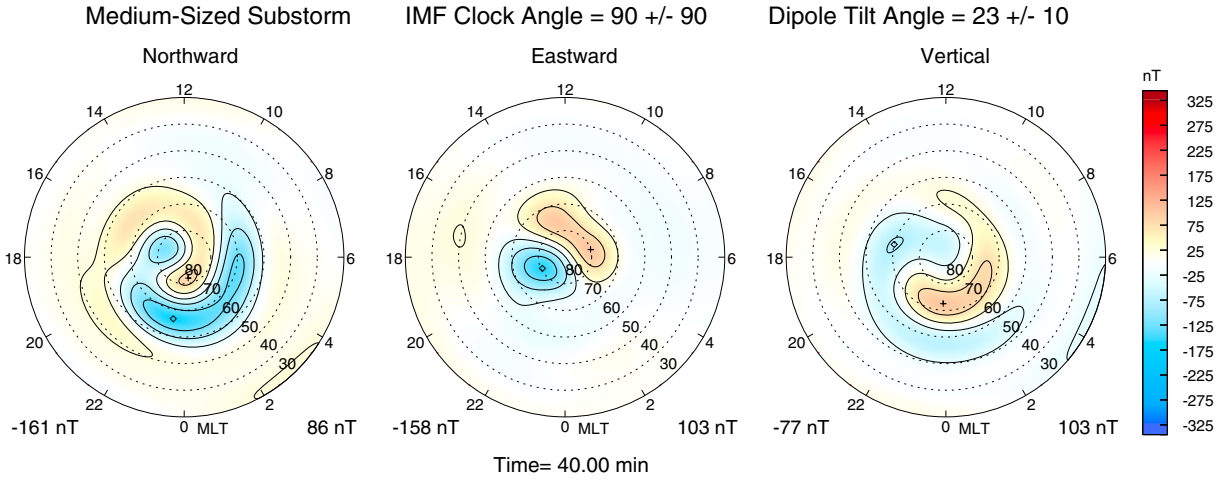

Figure 10. Maps of geomagnetic perturbations for a clock angle of 90° ($+B_Y$ IMF) and dipole tilt angle of +23° (summer). The format of the figure and the other data selection conditions are the same as in Figure 5.

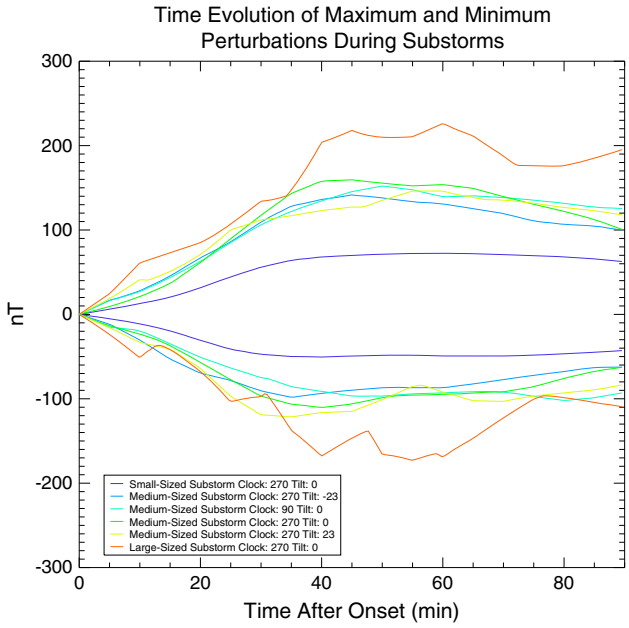

Figure 11. The time evolution of the maximum and minimum perturbations in the fits observed during substorms. Each color corresponds to a different category: Purple is for small substorms during the equinox with $-B_Y$ IMF, blue is for medium substorms during winter with $-B_Y$ IMF, cyan is for medium substorms during the equinox with $+B_Y$ IMF, green is for medium substorms during the equinox with $-B_Y$ IMF, yellow is for medium substorms during summer with $-B_Y$ IMF, and red is for large substorms during the equinox with $-B_Y$ IMF.

the fits at all times within each series, similarly to the static figures. Therefore, all maps of the perturbations start with zero everywhere when the time is zero, and their evolution shows the growth and decay of the substorm currents.

The differences due to seasonal effects can be examined in Animations S1–S3. The dominant features in the summer case (Animation S1) tend to be stronger and slightly less organized than in the equinox (Animation S2) and winter (Animation S3) cases, particularly for the eastward and vertical components. This follows what was observed in the static figures and also supports the significance of dipole tilt variations in the effects of substorm perturbations, especially in the summer case.

The differences due to the orientation of the IMF can be seen in Animations S2 and S4. Similar to the static figures, the differences due to IMF orientation for all three components are minimal, aside from the magnitudes of the most dominant features. The perturbations for the IMF $-B_Y$ case (Animation S2) are slightly more enhanced than in the IMF $+B_Y$ case (Animation S4). Again, this supports the idea that IMF orientation may not have much of an impact on perturbations due to substorms.

The differences due to the size of the substorm are displayed in Animations S5, S2, and S6 (small, medium, and large, respectively). These results are very intuitive; a larger substorm will produce larger perturbations that are more broadly distributed. This is true for all three components but especially for the northward and vertical components. The large substorm case (Animation S6) shows additional features when compared to the small (Animation S5) and medium (Animation S2) cases, particularly near 15 MLT. These features not only are much stronger in magnitude but extend significantly farther in latitude as well. Some midlatitude features may be artifacts of having fewer data points to fit in the large-magnitude cases.

A common feature that exists in all but one of the animations is a maximum negative perturbation in the northward component that is initially located in the auroral latitudes at premidnight that shifts with time to postmidnight. The exception is Animation S1 for the $-B_Y$ IMF, summer case, in which the perturbations at onset first appear near 1 MLT, before moving to premidnight and then back to postmidnight.

Finally, it was worthwhile to compare the time evolution of just the peak maximum and minimum values for each category to see if they fit the characteristic phases of substorm development. The maximum and minimum values from each animation were saved and plotted through time in Figure 11. From this figure, it is easy to see the differences in size of the substorms, but there are few differences among the other categories. It is also clear that the small- and medium-sized cases show what one would expect over the course of the substorm lifecycle. The large-magnitude group is more erratic, due to having fewer data points. It appears that the recovery phase in this group does not completely end before another growth phase begins after 75 min. These results may have some implications for future predictive models, as the small- and medium-sized substorms are very distinct.

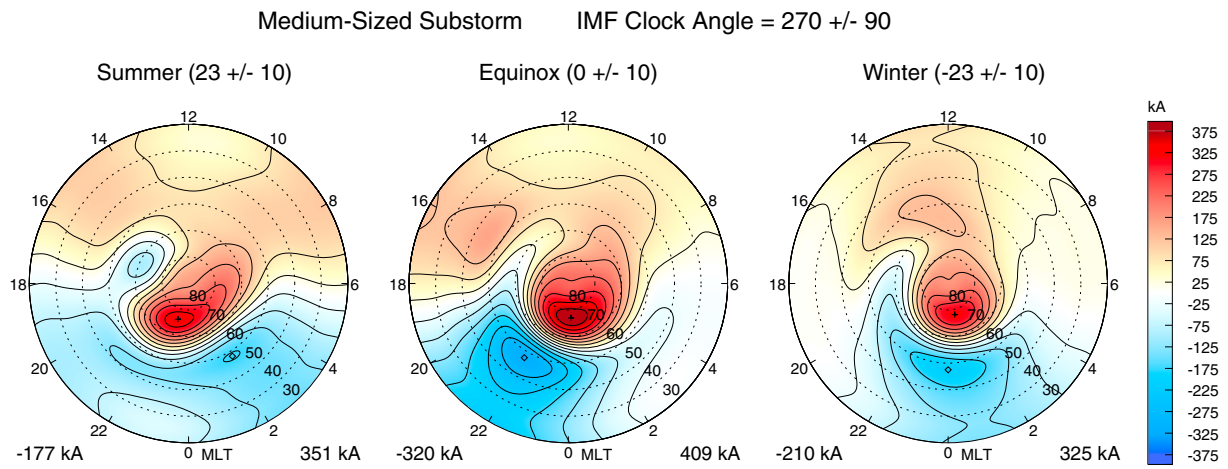

Figure 12. Equivalent current functions derived from magnetic perturbations. Three examples are shown, for summer, equinox, and winter tilt angles, having an IMF clock angle of 270° ($-B_Y$). These maps are derived from the patterns shown in Figures 9, 5, and 7.

4.4. Equivalent Currents

To facilitate a comparison with other results, it is useful to convert maps of the magnetic perturbations into ionospheric equivalent currents. Figure 12 shows three examples of the equivalent current function that is derived from the northward magnetic field mappings that are shown in Figures 5, 7, and 9. These examples have tilt angles that correspond to summer, equinox, and winter conditions, and an IMF clock angle of 270° ($-B_Y$). The signs of the contour levels match the same convention used in Figure 4 by *Richmond and Kamide* [1988]. The non-diverging, ionospheric Hall currents flow parallel to the contour lines, with their magnitude being proportional to the gradient in the perpendicular direction. The direction of current flow is clockwise around the positive peaks. The westward electrojet currents are very prominent in the close spacing of contour lines around midnight, at latitudes of 60–75°.

These maps were obtained by use of a magnetic potential. The gradient of this potential matches the horizontal magnetic field on the ground. The equivalent current function is derived from a spherical harmonic expansion for this magnetic potential through use of a formula given by *Chapman and Bartels* [1940]. Converting their equation (83) to MKS units, one obtains

$$J_k(r,\theta,\phi) = \frac{-1}{\mu_o}\sum_k \frac{2n_k+1}{n_k+1} W_k(a,\theta,\phi)\left(\frac{r}{a}\right)^{n_k} \quad (a<r) \tag{2}$$

where W_k represents the series expansion of the magnetic potential at the surface of the Earth, at radius a, and J_k represents the corresponding terms for the equivalent current function in the ionosphere, at radius r. As spherical cap harmonics are being used, the non-integer values $n_k(m)$ are substituted in place of the integer n. This formula is also used by *Haines and Torta* [1994]. For simplicity, the effects of underground currents have not been included in the calculation of these equivalent currents.

5. Discussion

The results presented here generally confirm previous work. During the peak of the substorm expansion phase, the northward component has a strong, negative perturbation in the auroral latitudes (50–70°) at premidnight (22–24 MLT) as shown in the left map of Figures 5–10. This strong southward directed perturbation near midnight is the expected signature for a substorm, and it matches the description of the DP 1 current system [*Obayashi and Nishida*, 1968; *Clauer and Kamide*, 1985]. A positive northward perturbation of lesser strength is evident at auroral latitudes near 15–16 MLT, corresponding to changes in the *AU** index during substorms. This change in *AU** may be related to a slight enhancement of the *DP* 2 current system after onset.

The southward perturbation at midnight corresponds to a strong westward electrojet, and it is located at the typical substorm onset region and the "auroral bulge" that is commonly seen by polar imagers [*Fujii et al.*, 1994].

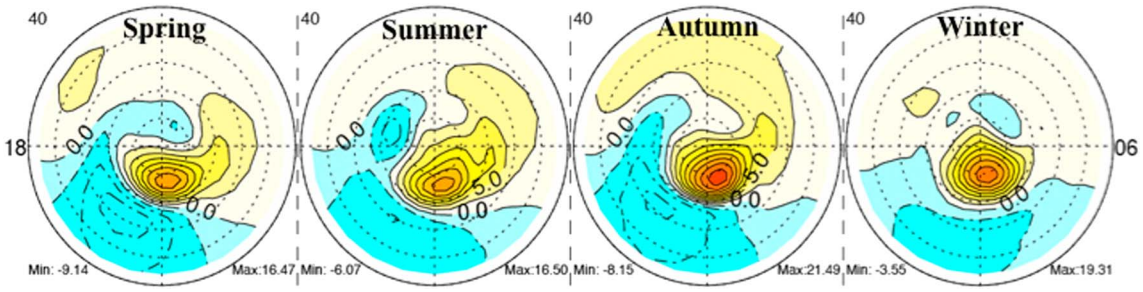

Figure 13. Averaged ionospheric residual potential patterns following substorm onset at 40 min following onset, for spring, summer, autumn, and winter, respectively. Diagram obtained from Figure 5b by *Cai et al.* [2006].

Prior to substorms, this negative peak is usually located at dawn, so our results explain the observation by *Gjerloev et al.* [2004] that "at substorm onset the *AL* contributing station makes a characteristic jump from a location near the dawn terminator to the onset region, typically bypassing one or more *AE* stations."

It is important to note that during the data selection for this project, it was not required that the most negative perturbations be located in a specific region, as only the *AU*/AL** signatures were examined for the substorm event selection. Since the results, including the scatterplots of the raw data measurements shown in Figures 4a and 4c, are in agreement with the classic substorm signature then it can be concluded a posteriori that the substorm event selection has worked as desired.

Another widely used definition of substorms requires that there is a positive perturbation in the northward component at midlatitudes, flanked by a positive eastward component premidnight and a westward perturbation postmidnight [*McPherron et al.*, 1973; *Clauer and McPherron*, 1974]. Again, although we did not require this signature in our event selection, this northward perturbation on the nightside at midlatitudes is seen in our results (Figures 5–10), as well as the slight eastward component that changes from positive to negative near midnight.

Regarding the vertical component, a persistent feature in our results that are found in the figures is that there is an area with prominent upward magnetic perturbation (vertical is positive downward in the Northern Hemisphere) between 50° and 65° latitude, premidnight, and a strong downward component poleward of this region. The latitude where the vertical field changes sign tends to be colocated with the peak in the southward magnetic field. In two of the three cases where the equivalent current functions have been graphed in Figure 12, the minimum and maximum values of the vertical components are located very close to the corresponding peaks in the current functions.

It is useful to compare these current functions with the results obtained by *Cai et al.* [2006]. They had derived the averaged ionospheric residual electric potential patterns following substorm onset, using the assimilative mapping of ionospheric electrodynamics technique. In their results, reproduced here in Figure 13, the electric potentials at their peaks have patterns that are similar to the maps of the vertical component of the geomagnetic perturbations, as observed in Figures 5–10. There is a negative peak in both the electric potential and the vertical magnetic field in the auroral latitudes near premidnight and a positive peak poleward of the negative region at about the same MLT. Similarly, there is a very close match between their electric potentials (Figure 13) and the equivalent ionospheric currents shown in Figure 12, the reason being that Hall currents flow along the equipotential lines.

We also find an excellent agreement between the current functions in Figure 12 and the results shown by *Gjerloev and Hoffman* [2014]. Our results show a similar westward electrojet that at premidnight is slightly poleward of the location on the postmidnight side. There are very prominent, circular cells near midnight, between 70° and 80°, corresponding to the "polar cap swirl" described by *Gjerloev and Hoffman* [2014]. The current lines in Figure 12 also turn equatorward between 20 and 22 MLT, just as they do in Figure 1.

Lastly, in both the static figures and animations, the latitude of the perturbations is slightly higher, by about a degree, in going from positive to negative tilt angles (moving from 68° to 69° approximately). This is likely due to the stretched-out magnetotail being below the magnetic dipole equator for summer tilt and above the magnetic dipole equator for winter tilt, therefore mapping to slightly lower and higher latitude, respectively.

6. Conclusions

Our results confirm the influence of dipole tilt angle on the geomagnetic response to substorms [*Wanliss,* 2006]. In comparison with the maps that illustrate the changes with dipole tilt angle, or season, the influence of IMF orientation is less noticeable in the contour graphs (Figures 5–10).

As evident from Figures 4a and 4c, many of the data from stations widely separated in geographic longitude are in very good local agreement where they overlap in MLT. The coherence in the patterns that are evident in these scatterplots on the left side is an indication that the mappings of the geomagnetic perturbations described here are robust and reproducible. This behavior will be very useful in building future predictive models of geomagnetic perturbations in response to substorm onset. The contour maps that have been developed should be useful to the space science community as a context for past and future observations, as well as theoretical predictions and validating numerical models.

Our results generally agree with features that are found in similar models describing changes in electric potentials [*Weimer*, 1999; *Cai et al.,* 2006] and ionospheric currents [*Gjerloev and Hoffman*, 2014]. One new result is the identification of a pattern in the vertical component, a downward magnetic field that is poleward of the westward electrojet and an upward field on the equatorward side, in the premidnight region. These features in the vertical magnetic field tend to be colocated with circular cells in the electric potentials and equivalent currents. At locations where these circular cells are present, it can also be assumed that diverging Pedersen currents are associated with field-aligned currents. On the basis of this evidence, we infer that vertical magnetic fields at ground level tend to be found underneath the locations where downward and upward field-aligned currents enter and exit the ionosphere. These vertical fields are produced by Hall currents, as it is well known that the FAC do not directly produce a magnetic field at the ground [*Fukushima*, 1976].

This work builds on the framework laid out by *Weimer et al.* [2010]. Their original database was extended an additional 4 years, for inclusion in the model developed by *Weimer* [2013]. The data presented here were selected to map the geomagnetic response specifically following substorm onset, which will aid in improving the accuracy of future predictive models. It should be pointed out that our maps are highly smoothed, and the greatest perturbations that are most important to forecasting can be considerably larger. It is well known that the aurora within substorms contains smaller-scale features, on the order of a few kilometers, that these features are more structured and dynamic. Since the peak magnetic field values are the result of random and chaotic small-scale fluctuations [*Pulkkinen et al.*, 2006], future work should focus on the determination of probabilities of experiencing a large fluctuation at a particular location and time.

Predictive models of surface geomagnetic perturbations in response to space weather events (including magnetospheric substorms) would be beneficial. *Pulkkinen et al.* [2011] showed that an early version of a model developed by *Weimer* [2013] did as well or better than numerical models in predicting large-scale ΔB perturbations from solar wind and IMF input. However, *Pulkkinen et al.* [2013] found that the model [*Weimer,* 2013] does not do as well in predicting the magnitude of ΔB at 1 min resolution. That is because this model does not reproduce rapid, auroral movements or include substorm modeling. With the addition of a substorm component, the geomagnetic predictions could be improved. The results shown here are the first step toward deriving the substorm perturbations that could be combined with the model output derived from the real-time solar wind measurements.

Accurate forecasting of these events will help to manage the exposure of essential assets to geomagnetic variations. The work presented here continues to make positive advancements toward the goal of producing such a predictive model but still requires a method to predict the timing of substorm onsets and their peak magnitudes.

Acknowledgments

N. Pothier gratefully acknowledges the NOAA CREST program for their financial support of this work. We thank the ground magnetometer observatories, including the International Real-time Magnetic observatory Network (INTERMAGNET), the Canadian Array for Real-time Investigations of Magnetic Activity (CARISMA; operated by the University of Alberta and funded by the Canadian Space Agency), Japan's "210 MM Magnetometer Network" (GM210), the European International Monitor for Auroral Geomagnetic Effects (IMAGE), the Magnetometer Array for Cusp and Cleft Studies (MACCS; supported by NSF grant ATM-0827903), the Greenland magnetometer array, the WDC_UK (World Data Center, United Kingdom), and the Alaska Geophysical Institute Magnetometer Array (GIMA), for maintaining and providing magnetometer data. We acknowledge the NASA National Space Science Data Center, the Space Physics Data Facility, and the ACE Principal Investigator, Edward C. Stone of the California Institute of Technology, for usage of ACE data that were obtained from nssdcftp.gsfc.nasa.gov. D. Weimer acknowledges support from NSF grants ATM-0817751 and AGS-1303116 and the NASA grant NNX09AJ58G to Virginia Tech.

Michael Liemohn thanks the reviewers for their assistance in evaluating this paper.

References

Amm, O. (1995), Direct determination of the local ionospheric Hall conductance distribution from two-dimensional electric and magnetic field data: Application of the method using models of typical ionospheric electrodynamic situation, *J. Geophys. Res.*, *100*(A11), 21,473–21,488, doi:10.1029/1995JA02213.

Amm, O. (2001), The elementary current method for calculating ionospheric current systems from multisatellite and ground magnetometer data, *J. Geophys. Res.*, *106*(A11), 24,843–24,855, doi:10.1029/2001JA900021.

Amm, O. (2002), Method of characteristics for calculating ionospheric electrodynamics from multisatellite and ground-based radar data, *J. Geophys. Res.*, *107*(A10), 1270, doi:10.1029/2001JA005077.

Amm, O., A. Aruliah, S. C. Buchert, R. Fujii, J. W. Gjerloev, A. Ieda, T. Matsuo, C. Stolle, H. Vanhamäki, and A. Yoshikawa (2008), Towards understanding the electrodynamics of the 3-dimensional high-latitude ionosphere: Present and future, *Ann. Geophys.*, *26*, 3913–3932.

Anderson, B. J., H. Korth, C. L. Waters, D. L. Green, and P. Stauning (2008), Statistical Birkeland current distributions from magnetic field observations by the Iridium constellation, *Ann. Geophys.*, *26*, 671–687.

Anderson, B. J., H. Korth, C. L. Waters, D. L. Green, V. G. Merkin, R. J. Barnes, and L. P. Dyrud (2014), Development of large-scale Birkeland currents determined from the Active Magnetosphere and Planetary Electrodynamics Response Experiment, *Geophys. Res. Lett.*, *41*, 3017–3025, doi:10.1002/2014GL059941.

Berthelier, A., J. J. Berthelier, and C. Guerin (1974), The effect of the east-west component of the interplanetary magnetic field on magnetospheric convection as deduced from magnetic perturbations at high latitudes, *J. Geophys. Res.*, *79*, 3187–3192, doi:10.1029/JA079i022p03187.

Boteler, D. H., R. J. Pirjola, and H. Nevanlinna (1998), The effects of geomagnetic disturbances on electrical systems at the Earth's surface, *Adv. Space Res.*, *22*(1), 17–27.

Cai, X., C. R. Clauer, and A. J. Ridley (2006), Statistical analysis of ionospheric potential patterns for isolated substorms and sawtooth events, *Ann. Geophys.*, *24*, 1977–1991.

Chapman, S., and J. Bartels (1940), *Geomagnetism, Vol. II, Analysis of the Data, and Physical Theories*, Oxford Univ. Press, London.

Christiansen, F., V. O. Papitashvili, and T. Neubert (2002), Seasonal variations of high-latitude field-aligned currents inferred from Ørsted and Magsat observations, *J. Geophys. Res.*, *107*(A2), 1029, doi:10.1029/2001JA900104.

Clauer, C. R., and Y. Kamide (1985), *DP* 1 and *DP* 2 current systems for the March 22, 1979 substorms, *J. Geophys. Res.*, *90*(A2), 1343–1354, doi:10.1029/JA090iA02p01343.

Clauer, C. R., and R. L. McPherron (1974), Mapping the local time-universal time development of magnetospheric substorms using mid-latitude magnetic observations, *J. Geophys. Res.*, *79*(19), 2811–2820, doi:10.1029/JA079i019p02811.

Clauer, C. R., R. L. McPherron, C. Searls, and M. G. Kivelson (1981), Solar wind control of auroral zone geomagnetic activity, *Geophys. Res. Lett.*, *8*(8), 915–918, doi:10.1029/GL008i008p00915.

Clauer, C., R. McPherron, and C. Searls (1983), Solar wind control of the low-latitude asymmetric magnetic disturbance field, *J. Geophys. Res.*, *88*(A3), 2123–2130, doi:10.1029/0JGREA0000880000A3002123000001.

Davis, T. N., and M. Sugiura (1966), Auroral electrojet activity index *AE* and its universal time variations, *J. Geophys. Res.*, *71*, 785–801, doi:10.1029/JZ071i003p00785.

De Zeeuw, D. L., S. Sazykin, R. A. Wolf, T. I. Gombosi, A. J. Ridley, and G. Tóth (2004), Coupling of a global MHD code and an inner magnetospheric model: Initial results, *J. Geophys. Res.*, *109*, A12219, doi:10.1029/2003JA010366.

Emmert, J. T., A. D. Richmond, and D. P. Drob (2010), A computationally compact representation of magnetic-apex and quasi-dipole coordinates with smooth base vectors, *J. Geophys. Res.*, *115*, A08322, doi:10.1029/2003JA010366.

Frey, H. U., S. B. Mende, and V. Angelopoulos (2004), Substorm onset observations by IMAGE-FUV, *J. Geophys. Res.*, *109*, A10304, doi:10.1029/2004JA010607.

Friis-Christensen, E., and J. Wilhjelm (1975), Polar cap currents for different directions of the interplanetary magnetic field in the *Y-Z* plane, *J. Geophys. Res.*, *80*(10), 1248–1260, doi:10.1029/JA080i010p01248.

Friis-Christensen, E., K. Lassen, J. Wilhjelm, J. M. Wilcox, W. Gonzalez, and D. S. Colburn (1972), Critical component of the interplanetary magnetic field responsible for large geomagnetic effects in the polar cap, *J. Geophys. Res.*, *77*(19), 3371–3376, doi:10.1029/JA077i019p03371.

Friis-Christensen, E., Y. Kamide, A. D. Richmond, and S. Matsushita (1985), Interplanetary magnetic field control of high-latitude electric fields and currents determined from Greenland magnetometer data, *J. Geophys. Res.*, *90*(A2), 1325–1338, doi:10.1029/JA090iA02p01325.

Fujii, R., R. A. Hoffman, P. C. Anderson, J. D. Craven, M. Sugiura, L. A. Frank, and N. C. Maynard (1994), Electrodynamic parameters in the nighttime sector during auroral substorms, *J. Geophys. Res.*, *99*(A4), 6093, doi:10.1029/93JA02210.

Fukushima, N. (1976), Generalized theorem for no ground magnetic effect of vertical currents connected with Pedersen currents in the uniform-conductivity ionosphere, *Report of Ionosphere and Space Research in Japan*, *30*(1–2), pp. 35–40.

Gjerloev, J. W., and R. A. Hoffman (2002), Currents in auroral substorms, *J. Geophys. Res.*, *107*(A8), 1163, doi:10.1029/2001JA000194.

Gjerloev, J. W., and R. A. Hoffman (2014), The large-scale current system during auroral substorms, *J. Geophys. Res. Space Physics*, *119*, 4591–4606, doi:10.1002/2013JA019176.

Gjerloev, J. W., R. A. Hoffman, M. M. Friel, L. A. Frank, and J. B. Sigwarth (2004), Substorm behavior of the auroral electrojet indices, *Ann. Geophys.*, *22*, 2135.

Gjerloev, J. W., R. A. Hoffman, J. Sigwarth, and L. A. Frank (2007), Statistical description of the bulge-type auroral substorm in the far ultra-violet, *J. Geophys. Res.*, *112*, A07213, doi:10.1029/2006JA012189.

Gleisner, H., and H. Lundstedt (2001), A neural network-based local model for prediction of geomagnetic disturbances, *J. Geophys. Res.*, *106*(A5), 8425, doi:10.1029/2000JA900142.

Haaland, S. E., G. Paschmann, M. Forster, J. M. Quinn, R. B. Torbert, C. E. McIlwain, H. Vaith, P. A. Puhl-Quinn, and C. A. Kletzing (2007), High-latitude plasma convection from Cluster EDI measurements: Method and IMF-dependence, *Ann. Geophys.*, *25*, 239–253.

Haines, G. V. (1985), Spherical cap harmonic analysis, *J. Geophys. Res.*, *90*(B3), 2583–2591, doi:10.1029/JB090iB03p02583.

Haines, G. V., and J. M. Torta (1994), Determination of equivalent current sources from spherical cap harmonic models of geomagnetic field variations, *Geophys. Res. Int.*, *118*, 499–514.

Hapgood, M. A. (1992), Space physics coordinate transformations: A user guide, *Planet. Space Sci.*, *40*, 711–717.

Heppner, J. P., and N. C. Maynard (1987), Empirical high-latitude electric field models, *J. Geophys. Res.*, *92*(A5), 4467–4489, doi:10.1029/JA092iA05p04467.

Hsu, T.-S., and R. L. McPherron (2002), An evaluation of the statistical significance of the association between northward turnings of the IMF and substorm expansion onsets, *J. Geophys. Res.*, *107*(A11), 1398, doi:10.1029/2000JA000125.

Jørgensen, T. S., E. Friis-Christensen, and J. Wilhjelm (1972), Interplanetary magnetic-field direction and high-latitude ionospheric currents, *J. Geophys. Res.*, *77*(10), 1976–1977, doi:10.1029/JA077i010p01976.

Kamide, Y., and S. Kokubun (1996), Two-component auroral electrojet: Importance for substorm studies, *J. Geophys. Res.*, *101*(A6), 13,027–13,046, doi:10.1029/96JA00142.

Lam, H.-L., D. H. Boteler, and L. Trichtchenko (2002), Case studies of space weather events from their launching on the Sun to their impacts on power systems on the Earth, *Ann. Geophys.*, *20*, 1073–1079, doi:10.5194/angeo-20-1073-2002.

Lanzerotti, L. J. (1979), Geomagnetic influences on man-made systems, *J. Atmos. Terr. Phys.*, *41*, 787–796.

Liou, K., P. T. Newell, D. G. Sibeck, and C.-I. Meng (2001), Observation of IMF and seasonal effects in the location of auroral substorm onset, *J. Geophys. Res.*, *106*(A4), 5799–5810, doi:10.1029/2000JA003001.

Mayaud, P. N. (1980), *Derivation, Meaning, and Use of Geomagnetic Indices*, *Geophys. Monogr. Ser.*, vol. 22, 154 pp., AGU, Washington, D. C., doi:10.1029/GM022.

McPherron, R. L., C. T. Russell, and M. P. Aubry (1973), Satellite studies of magnetospheric substorms on August 15, 1968: Phenomenological model for substorms, *J. Geophys. Res.*, *78*(16), 3131–3149, doi:10.1029/JA078i016p03131.
Newell, P. T., and J. W. Gjerloev (2011), Evaluation of SuperMAG auroral indices as indicators of substorms and auroral power, *J. Geophys. Res.*, *116*, A12211, doi:10.1029/2011JA016936.
Nishida, A. (1968a), Geomagnetic D_p 2 fluctuations and associated magnetospheric phenomena, *J. Geophys. Res.*, *73*(5), 1795–1803, doi:10.1029/JA073i005p01795.
Nishida, A. (1968b), Coherence of geomagnetic *DP* 2 fluctuations with interplanetary magnetic variations, *J. Geophys. Res.*, *73*(17), 5549–5559, doi:10.1029/JA073i017p05549.
Nowada, M., J.-H. Shue, and C. T. Russell (2009), Effects of dipole tilt angle on geomagnetic activity, *Planet. Space Sci.*, *57*, 1254–1259.
Obayashi, T. (1967), The interaction of solar plasma with geomagnetic field, disturbed condition, in *Solar Terrestrial Physics*, edited by J. W. King and W. S. Newman, 107 pp., Academic Press, London and New York.
Obayashi, T., and A. Nishida (1968), Large-scale electric field in the magnetosphere, *Space Sci. Rev.*, *8*, 3.
Opgenoorth, H. J., R. J. Pellinen, W. Baumjohann, E. Nielsen, G. Marklund, and L. Eliasson (1983), Three-dimensional current flow and particle precipitation in a westward travelling surge (observed during the Barium-GEOS rocket experiment), *J. Geophys. Res.*, *88*(A4), 3138–3152, doi:10.1029/JA088iA04p03138.
Østgaard, N., S. B. Mende, H. U. Frey, T. J. Immel, L. A. Frank, J. B. Sigwarth, and T. J. Stubbs (2004), Interplanetary magnetic field control of the location of substorm onset and auroral features in the conjugate hemispheres, *J. Geophys. Res.*, *109*, A07204, doi:10.1029/2003JA010370.
Papitashvili, V. O., F. Christiansen, and T. Neubert (2002), A new model of field-aligned currents derived from high-precision satellite magnetic field data, *Geophys. Res. Lett.*, *29*(14), 1683, doi:10.1029/2001GL014207.
Pulkkinen, A., A. Thomson, E. Clarke, and A. McKay (2003), April 2000 geomagnetic storm: Ionospheric drivers of large geomagnetically induced currents, *Ann. Geophys.*, *21*, 709–717.
Pulkkinen, A., A. Klimas, D. Vassiliadis, V. Uritsky, and E. Tanskanen (2006), Spatiotemporal scaling properties of the ground geomagnetic field variations, *J. Geophys. Res.*, *111*, A03305, doi:10.1029/2005JA011294.
Pulkkinen, A., M. Hesse, M. Kuznetsova, and L. Rastatter (2007), First-principles modeling of geomagnetically induced electromagnetic fields and currents from upstream solar wind to the surface of the Earth, *Ann. Geophys.*, *25*, 881–893.
Pulkkinen, A., et al. (2011), Geospace Environment Modeling 2008–2009 Challenge: Ground magnetic field perturbations, *Space Weather*, *9*, S02004, doi:10.1029/2010SW000600.
Pulkkinen, A., et al. (2013), Community-wide validation of geospace model ground magnetic field perturbation predictions to support model transition to operations, *Space Weather*, *11*, 369–385, doi:10.1002/swe.20056.
Raeder, J., R. L. McPherron, L. A. Frank, S. Kokubun, G. Lu, T. Mukai, W. R. Paterson, J. B. Sigwarth, H. J. Singer, and J. A. Slavin (2001), Global simulation of the Geospace Environment Modeling substorm challenge event, *J. Geophys. Res.*, *106*(A1), 381–396, doi:10.1029/2000JA000605.
Rich, F. J., and M. Hairston (1994), Large-scale convection patterns observed by DMSP, *J. Geophys. Res.*, *99*(A3), 3827–3844, doi:10.1029/93JA03296.
Richmond, A. D., and Y. Kamide (1988), Mapping electrodynamic features of the high-latitude ionosphere from localized observations: Technique, *J. Geophys. Res.*, *93*(A6), 5741, doi:10.1029/JA093iA06p05741.
Ruohoniemi, J., and R. Greenwald (1996), Statistical patterns of high latitude convection obtained from Goose Bay HF radar observations, *J. Geophys. Res.*, *101*, 21,743–21,763, doi:10.1029/96JA01584.
Tanskanen, E. I., T. I. Pulkkinen, A. Viljanen, K. Mursula, N. Partamies, and J. A. Slavin (2011), From space weather toward space climate time scales: Substorm analysis from 1993 to 2008, *J. Geophys. Res.*, *116*, A00I34, doi:10.1029/2010JA015788.
Vennerstrøm, S., and E. Friis-Christensen (1987), On the role of IMF B_y in generating the electric field responsible for the flow across the polar cap, *J. Geophys. Res.*, *92*(A1), 195–202, doi:10.1029/JA092iA01p00195.
Viljanen, A., E. I. Taskanen, and A. Pulkkinen (2006), Relation between substorm characteristics and rapid temporal variations of the ground magnetic field, *Ann. Geophys.*, *24*, 725–733.
Wanliss, J. (2006), Substorm onset location and dipole tilt angle, *Ann. Geophys.*, *24*, 577–588, doi:10.5194/angeo-24-577-2006.
Weigel, R. S., D. Vassiliadis, and A. J. Klimas (2002), Coupling of the solar wind to temporal fluctuations in ground magnetic fields, *Geophys. Res. Lett.*, *29*(19), 1915, doi:10.1029/2002GL014740.
Weimer, D. R. (1994), Substorm time constants, *J. Geophys. Res.*, *99*(A6), 11,005–11,015, doi:10.1029/93JA02721.
Weimer, D. R. (1999), Substorm influence on the ionospheric electric potentials and currents, *J. Geophys. Res.*, *104*(A1), 185–197, doi:10.1029/1998JA900075.
Weimer, D. R. (2001), An improved model of ionospheric electric potentials including substorm perturbations and application to the GEM November 24, 1996 event, *J. Geophys. Res.*, *106*, 407–416, doi:10.1029/2000JA000604.
Weimer, D. R. (2013), An empirical model of ground-level geomagnetic perturbations, *Space Weather*, *11*, 107–120, doi:10.1002/swe.20030.
Weimer, D. R., C. R. Clauer, M. J. Engebretson, T. L. Hansen, H. Gleisner, I. Mann, and K. Yumoto (2010), Statistical maps of geomagnetic perturbations as a function of the interplanetary magnetic field, *J. Geophys. Res.*, *115*, A10320, doi:10.1029/2010JA015540.
Wiltberger, M., S. R. Elkington, T. Guild, D. N. Baker, and J. G. Lyon (2005), Comparison of MHD simulations of isolated and storm time substorms, in *Inner Magnetosphere: Physics and Modeling*, *Geophys. Monogr. Ser.*, vol. 155, pp. 271–281, AGU, Washington, D. C.